ADVANCED MATERIALS TECHNOLOGIES

Tailored Design-of-Experiments Approach for Device Performance Prediction and Optimization of Flash-Evaporated Organic–Inorganic Halide Perovskite-Based Photodetectors

Jonghoon Lee, Woocheol Lee, Jeongjae Lee, Kyeong-Yoon Baek, Jiwon Shin, Jae-Keun Kim, Junwoo Kim, Heebeom Ahn, Keehoon Kang,* and Takhee Lee*

Single-source flash evaporation method has recently gained attention for its potential as a rapid and solvent-free deposition method for producing organic–inorganic halide perovskite (OHP) films in large-scale. However, due to a complex nature of the different experimental parameters involved in the deposition process, it is not straightforward to obtain the optimal condition for producing high-quality OHP films. In this study, this problem is tackled by employing the design-of-experiment (DoE) process, which is an efficient statistical analysis for finding an optimized condition with a minimized number of experiments. The DoE process is used for optimizing the responsivity of the OHP photodetector devices against the input variables used in the deposition that yielded an enhanced responsivity of 112.2 mA W^{-1}, which is up to an order of magnitude higher than that of the unoptimized devices. The experimental results using the DoE method provide not only the conditions required for enhancing the device performance but also the guidelines for improving the overall film quality through exploring the variable space of the flash evaporation technique.

1. Introduction

Organic–inorganic halide perovskites (OHPs) have recently received enormous attention due to their excellent properties for optoelectronic[1–3] and electronic[4,5] devices. Out of various deposition methods studied in the field, solution-processing,[1b,5a] chemical vapor deposition (CVD),[6] and thermal evaporation[7] have gained the most attention for OHPs. Spin-coating techniques of OHPs are mainly used in lab-scale device fabrication

because it is a low-cost and easily accessible process. Although some works have reported remarkable device performances in large-area perovskite optoelectronic devices made with spin-coated perovskite films,[2c,8] the spin-coating techniques face a challenge in producing reliable and uniform films over a large area. On the other hand, evaporation methods,[9] which include dual-source vacuum deposition,[10] sequential-partial pressure,[11] mixed solution and vapor deposition,[12] modified chemical vapor deposition method,[11] and single-source deposition,[13] have shown a potential for producing uniform films over a large area.[9,12] The evaporation methods do not require the use of solvents and thus have the advantage that the films can be deposited without solvent-induced-damages which are critical for organo-metal-halide perovskite films.[14]

Organo-halide precursor (e.g., methylammonium iodide, MAI) and lead-source precursor (e.g., lead iodide, PbI$_2$) can be thermally evaporated by various methods, i.e., coevaporation method,[7a,15] vapor-assisted deposition,[3a,16] or sequential deposition[17] to fabricate OHP (e.g., methylammonium lead iodide, MAPbI$_3$) films. Although these deposition methods are well-established, it is crucial to produce OHP films with the desired stoichiometric ratio among the three different ionic components by evaporation because each precursor has different sublimation temperatures.[9]

The single-source flash evaporation method[7b,13,14b,18] has gained attention as a candidate for thermally evaporating from either a mixed-precursor source or presynthesized stoichiometric OHP source by expeditiously raising the temperature in a short time. In principle, the rapid vaporization of the single crystal precursors results in a uniform and homogeneous evaporation of the precursors while maintaining the same ratio between the different components in OHP.[14b] Furthermore, the single-source flash evaporation method can be expanded to fabricate OHP films with mixed cation and halide species, which is challenging in other methods.[9] Although these aspects of the single-source flash evaporation present potential of exploring a diverse compositional range of OHPs, there has

J. Lee, W. Lee, Dr. J. Lee, K.-Y. Baek, J. Shin, J.-K. Kim, J. Kim, H. Ahn, Dr. K. Kang, Prof. T. Lee
Department of Physics and Astronomy, and Institute of Applied Physics
Seoul National University
Seoul 08826, Korea
E-mail: keehoon.kang@snu.ac.kr; tlee@snu.ac.kr
Dr. J. Lee
School of Earth and Environmental Sciences
Seoul National University
Seoul 08826, Korea

**ADVANCED
SCIENCE NEWS**

www.advancedsciencenews.com

**ADVANCED
MATERIALS
TECHNOLOGIES**

www.advmattechnol.de

been relatively few reports which have systematically studied the film quality optimization by considering the relationship between relevant input and response variables of the flash evaporation method.

The one-factor-at-a-time (OFAT) method, which is commonly used as a systematic experimental method, has clear disadvantages that it is relatively time-consuming and does not consider interaction effects because only one input variable is considered at a time. Moreover, most of the experimental designs typically require a long time to gather a sufficiently large training data set. Even after the model is completed, precise data predictions are limited to the variables within the range of the training data set. In this way, the effects of single input variables, e.g., substrate temperature,[19] excess amount of MAI, and chamber pressure[13] on the resulting film quality of the evaporated OHP films have been previously studied by following the OFAT method. However, multivariable interactions and correlations between the input and response variables for achieving desired film properties have not yet been investigated, to the best of our knowledge.

On the contrary, the design-of-experiment (DoE) approach[20] is a multivariate statistical method that is optimized for minimal experimentation. In addition, the DoE method allows us to consider the correlation between the variables in the analysis step and discover optimal experimental conditions via regression analysis. Because the DoE approach considers various variables simultaneously, it is an efficient tool for achieving experimental targets in a relatively short period of time, given that a clear objective is set. Although the DoE approach remains as a powerful tool for performing multivariate statistical analysis, it has been rarely used for investigating the film deposition conditions of organo-metal-halide perovskites.[21]

In our study, the DoE approach was used to analyze the relationship between the variables that affect the film deposition in the flash evaporation method, which in turn, provided guidelines for optimizing the deposition conditions that produce high-quality perovskite films with the desired optoelectronic properties. Our developed flash evaporation method was recently shown to be highly reproducible[22] and only had few control variables, both of which are suitable for employing the DoE approach for optimizing the film quality. In the analysis process, we first investigated the input variables that affect the physical and optoelectronic properties of the deposited perovskite films and extracted the relationships between these properties. By extending the film characterizations to photodetector devices, the DoE method was able to predict the responsivity values, which allowed us to design devices with a high responsivity value that was up to an order of magnitude higher than that of the devices fabricated from off-optimum conditions.

2. Result and Discussion

The overall stages of DoE method can be best described as sequential procedures that consist of 1) planning the experiments, 2) executing the experiments, 3) analyzing the results, and 4) optimizing via data analysis (see Figure S1 in the Supporting Information). In the stage of planning the experiments, input variables, response variables, and experimental

design are chosen according to the set objective. In this study, we employed response surface method (RSM) out of various experimental designs (see Section S2 in the Supporting Information for detail of DoE design) which is suited for optimizing deposition conditions for producing high-quality flash-evaporated MAPbI$_3$ films.[23] Among the RSM designs, the Box–Behnken design was chosen because it is an efficient design that needs relatively few numbers of experiments for optimization. It acquires data that correspond to experiments at the center of each side of the cubic variable space[24] (see **Figure 1**a). The length of each side of the cube represents a range of input variables and each point at the center (represented as circles in Figure 1a) corresponds to a set of input variables (i.e., an experimental condition) used for each experiment. In the Box–Behnken design, when three input variables are selected, 13 different experimental conditions are determined, and the center point experiment condition (dark blue circle in Figure 1a) is repeatedly evaluated three times to verify reproducibility and robustness of the model. By using such an experimental model, the experiments are arranged regularly such that potential bias toward specific experimental conditions is avoided. Therefore, it is a convenient model to analyze the effect of individual input variables on each response variable, as well as the interactions between them.

The objective of the DoE process was to find the optimal deposition condition for single-source flash evaporation of MAPbI$_3$ film (from the set-up schematically drawn in Figure 1b) that results in high-performance photodetectors. In total, three input variables were selected based on the previous studies on flash evaporation of OHP films.[22] An excess amount of MAI added to the source (i.e., an excess molar ratio of MAI to MAPbI$_3$ powder) was selected as the first variable because it has been reported to play a role in reducing PbI$_2$ impurity in the evaporated film which is related to the relative purity of the evaporated film.[13] The other input variables were the mass of MAPbI$_3$ single crystal source (source mass, the second variable)[22] and the heating current (related to the heating temperature, the third variable)[7b,25] which control the total amount of evaporated materials and sublimation rate, both of which affect the thickness and grain size of the deposited MAPbI$_3$ films. By combining these three input variables that control the relative purity, grain size, and thickness of the MAPbI$_3$ films, we attempted to find out the relationships between physical properties, optoelectronic properties, and the resulting device performance of photodetectors made with the flash-evaporated MAPbI$_3$ films.

In the DoE process, the selection of the evaluation scope, which is expressed as the size of the variable cube shown in Figure 1a, is important because we can extract the effect of multi-input-variables on each response variable, and thus find out optimum experimental condition within the evaluated range of the variables. The range of the input variables should be selected such that it is neither too wide to prevent an accurate linear regression analysis nor too narrow to risk the loss of generality of the extracted model. As a 1:1 molar ratio between MAI and MAPbI$_3$ was found to be ideal for reducing PbI$_2$ impurity in a previous study,[13] the evaluation range was selected from 0.5 to 1.5 mol ratio. In order to control the range of thickness from 500 to 2000 Å, the source mass (the second variable)
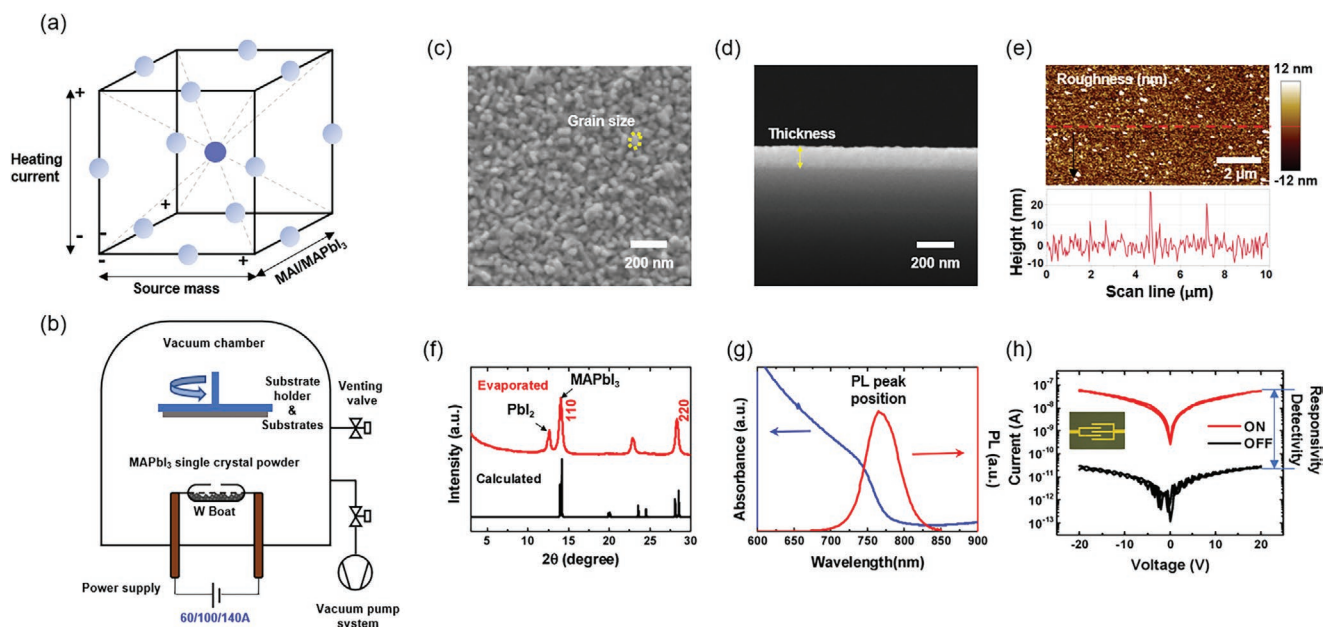
Figure 1. a) A graphical representation of the Box–Behnken design for three factors (heating current, source mass, and excess MAI ratio). b) A schematic illustration of single-source flash evaporation to deposit a MAPbI₃ film. c) Surface and d) cross-sectional SEM images, and e) an AFM image of the flash-evaporated MAPbI₃ film. f) X-ray diffraction pattern of the flash-evaporated MAPbI₃ film (red) and calculated data (black) from the unit cell of MAPbI₃. g) UV–visible absorbance spectra (blue) and PL spectra (red) of the MAPbI₃ film h) I–V characteristics of flash-evaporated perovskite photodetectors under white light illumination (red) and dark (black) conditions, which were used to extract responsivity (R) and specific detectivity (D*).

was evaluated in the range from 250 to 750 mg. For the heating current (the third variable), 60 A represented a slow sublimation of the source, nearly approaching the rate of conventional thermal evaporation. Therefore, the heating current was evaluated in the range between 60 and 140 A. In order to find out the effect of the aforementioned input variables, various physical and optoelectronic properties were measured. The measured properties were chosen as the response variables used to perform the multivariate analysis. The selected response variables are various film properties: grain size, thickness, roughness, relative purity, and photoluminescence (PL) peak position and photodetector device properties: responsivity and specific detectivity (Figure 1c–h).

Here, we show how we characterized each response variable by outlining the results for the evaporated film under the central condition, defined by the variable coordinate of 500 mg (source mass), 100 A (heating current), and 1.0 mol ratio (excess MAI ratio). First, the structural properties were probed by microscopy and X-ray diffraction (XRD) measurements. The resulting evaporated MAPbI₃ film had a grain size of ≈37 nm (σ: 7.2 nm) and a thickness of 133.3 nm (σ: 3.8 nm) as determined from the top-surface image and cross-sectional image measured with field-emission scanning electron microscope (FE-SEM) (Figure 1c,d). The grain size and thickness were averaged after measuring 20 locations in an image. The surface morphology of the film was probed by measuring the root-mean-squared value of surface roughness (Rq), which was measured to be 1.8 nm by atomic force microscope (AFM) (Figure 1e). Next, we used XRD data to determine the relative purity. Before discussing the relative purity, please note that the XRD data show good crystallinity of the MAPbI₃ film. XRD data showed peaks at 14.0° and 28.0° (2q) that coincide with (110) and (220) diffraction peaks of

the predicted MAPbI₃ results (Figure 1f). In addition, to determine the relative purity of the film, Rietveld refinement[26] was used to quantitatively estimate the amount of PbI₂ present in the MAPbI₃ film (Figure S3 in the Supporting Information) from the XRD data. Since the ratio of PbI₂ in the MAPbI₃ film is proportional to the XRD peak intensity, we defined the relative purity of the films with the following formula

$$\text{Relative purity} = \ln\left(\frac{I_{\text{MAPbI}_3}\,(14.0°)}{I_{\text{PbI}_2}\,(12.6°)}\right) \tag{1}$$

where $I_{\text{MAPbI}_3}\,(14.0°)$ and $I_{\text{PbI}_2}\,(12.6°)$ represent the XRD peak intensity at 14.0° and 12.6° that correspond to MAPbI₃ and PbI₂, respectively. Second, the photophysical properties of the MAPbI₃ film were measured by PL and UV–vis absorbance spectra to determine the wavelengths of the emission peak and absorption edge, respectively. The PL peak position appeared at near 765 nm which is identical to the expected results from previous studies[18a,27] and UV–vis absorbance edge appeared at 758 nm (Figure 1g).

Two of the most important response variables of interest can be the device performance parameters of the photodetectors fabricated with the flash-evaporated MAPbI₃ film. They are the responsivity (R) which represents a quantitative measure of how much excess electrical current output comes out when illuminated with light input and specific detectivity (D*) corresponding to the magnitude of the signal to noise ratio of a photodetector per unit bandwidth and unit area. In detail, the responsivity and specific detectivity are determined by $R = (I_{\text{light}} - I_{\text{dark}})/(PA)$ and $D^* = R\left(\frac{A}{2eI_{\text{dark}}}\right)^{\frac{1}{2}}$, respectively, where I_{light} is the current under illumination, I_{dark} is the dark current,

ADVANCED
SCIENCE NEWS
www.advancedsciencenews.com

ADVANCED
MATERIALS
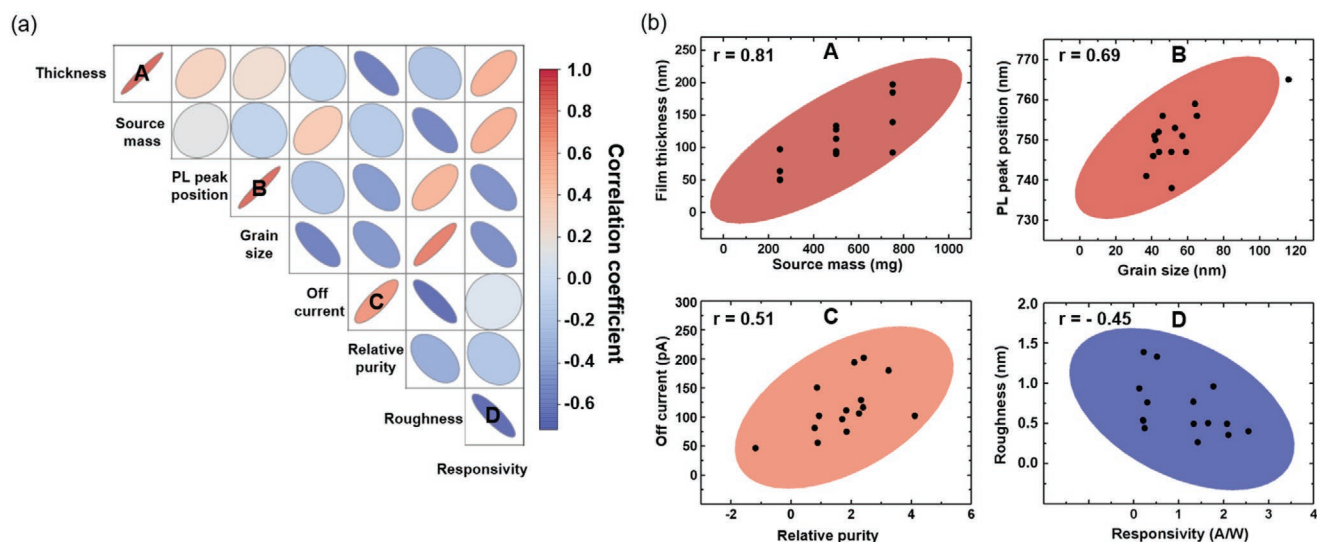**TECHNOLOGIES**
www.advmattechnol.de

Figure 2. a) Multivariable correlation matrix plot. b) Representative correlation graphs for source mass and film thickness, grain size, and PL peak position, relative purity and off current, and responsivity and surface roughness. The ellipses in the graphs show the regions with the confidence level of 90%.

P is the light intensity, A is the area of photosensitive region of the OHPs film, and e is the electric charge.[3d,28] The calculated responsivity of the device made with the film deposited under the central condition was found to be 57.8 mA W^{-1} (σ: 8.4 mA W^{-1}) (at the applied voltage of 20 V and incident light power of 424 nW) and the specific detectivity was found to be 1.8×10^{11} Jones (σ: 4.6×10^{10} Jones).

We now explain how the response variables mentioned above were analyzed via the DoE approach to study the correlation between each structural and photophysical property of the evaporated films, which later can be related to the device performances. A total of 15 experiments were conducted (Table S1, Supporting Information) with 13 different types of perovskite films made for each condition specified in Figure 1a. Before the regression analysis was conducted, the correlation matrix plot was used to understand the correlation between the variables, which were quantitatively estimated through the value of correlations (**Figure 2**a). The correlation matrix plot which is a set of scattering plots between variables provides a simple and holistic approach to check the relationships between the variables before performing detailed regression analysis. The correlations were analyzed by extracting the density ellipse for pairs of each input and response variable. The density ellipse displays the area that contains 90% of the total data in Figure 2b. When 13 numerical variables were analyzed by the correlation matrix plot (Figure S4 and Table S2, Supporting Information), the correlation matrix plot in Figure 2a, which consists of eight variables, could be expressed to focus on a set of variables with a significant degree of correlation. The following four correlation results were aligned with our expectations: the thickness of the deposited film increased as the source mass increased, as expected (plot A in Figure 2b). The wavelength of the PL peak position increased as the grain size increased (plot B in Figure 2b). This redshift in the PL emission as larger grain size is related to photon-reabsorption of emitted light in larger crystal grains, as reported previously.[29] The higher the relative purity, the larger the dark (off) current (plot C in Figure 2b),

which is related to PbI_2 acting as a charge-intercept barrier[30] (i.e., the dark current increased as the relative proportion of PbI_2 decreased). The responsivity decreased when the film surface became rougher (plot D in Figure 2b). A smooth morphology is likely to improve the charge transport which can lead to improved photoconductive gain, and therefore a larger photocurrent.[31] Although there is no absolute standard for the correlation coefficient (r) categorization, the r value falling within the range between 0.68 and 1.0 (plot A and B in our case) can be generally considered to indicate a strong correlation, and the range between 0.36 and 0.67 (plot C and D in our case) a moderate correlation.[32]

There were nontrivial correlation results that could be identified with the correlation analysis such as relatively strong correlations between heating current versus off current (+, positive correlation), PL intensity versus thickness (+), grain size versus roughness (+), and PL intensity versus responsivity (+) (Figure S5, Supporting Information) and the weak correlations between excess MAI ratio versus thickness, MAI ratio versus grain size, relative purity versus responsivity, and relative purity versus specific detectivity (Figure S6, Supporting Information). Although some of these weak correlation results were unexpected (e.g., excess MAI ratio versus thickness/grain size and relative purity versus responsivity/specific detectivity), we could build upon these simple correlation analyses to examine the most relevant factors for optimizing the photodetector device performance parameters by performing detailed regression analyses.

Before going into the regression analysis step, it is necessary to verify the reproducibility of the results to confirm the robustness of the experimental environment. We checked the reproducibility by comparing the three experiments performed for the central condition and re-evaluated additional conditions in the DoE cube (Table S1, Supporting Information). The data clearly show the reproducibility of the thickness, grain size, relative purity, and responsivity under the central condition and an additional DoE Condition (Table S3, Supporting Information).
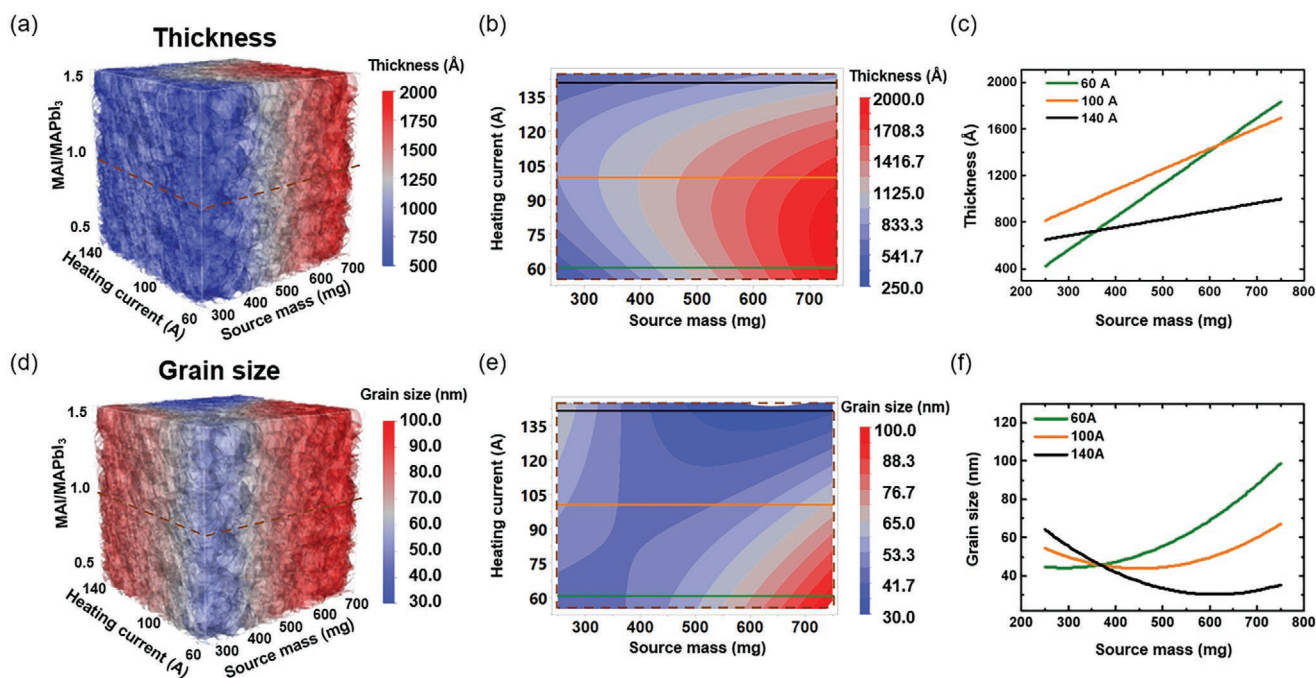
**ADVANCED
SCIENCE NEWS**

www.advancedsciencenews.com

**ADVANCED
MATERIALS
TECHNOLOGIES**

www.advmattechnol.de

Figure 3. a) A 3D scattering plot of the film thickness according to the heating current, source mass, and excess MAI ratio (MAI/MAPbI$_3$) from the regression analysis. b) A contour plot of the film thickness according to the heating current and the source mass. c) Graphs of the film thickness as a function of the source mass at the different heating currents of 60 A (green line), 100 A (orange line), and 140 A (black line). d–f) The same graphs as a–c) but represent the grain size instead of the film thickness.

The DoE approach, which analyzes data from multiple angles, can reduce misinterpretation by considering the interactions that can be overlooked in the optimizing process by OFAT method. Through regression analysis, each response variable can be quantitatively associated as a function of input variables to derive meaningful relationships between various film properties and device performance. The detailed regression analysis process is described in Section S8 (Supporting Information).[33] The regression analysis was performed on seven response variables-grain size, thickness, roughness, relative purity, PL peak position, responsivity, and specific detectivity- which revealed that grain size, thickness, relative purity, and responsivity values could be modeled well with input variables (Table S4, Supporting Information). On the other hand, the accuracy of modeling roughness, PL peak position, and specific detectivity was relatively low, and therefore these variables were excluded from the subsequent analysis.

For each response variable, we can represent the regression model as a 3D scattering plot with the axes and range corresponding to the input variable cube shown in Figure 1a. In the case of the thickness (**Figure 3**a), if we examine a cross-section from the 3D scattering plot perpendicularly to the excess MAI ratio axis at MAI/MAPbI$_3$ ratio of 1 (shown as the brown dashed line in Figure 3a), a 2D contour plot can be extracted with the source mass and heating current (Figure 3b). If we look closely at the lines along with the heating current values of 60 A (green line in Figure 3b), 100 A (orange), and 140 A (black), the thickness increases linearly with the source mass for all the current values (Figure 3c). However, the slope of the increase in the thickness varies according to the heating current: the lower the heating current, the larger the slope. This is an example of an

interaction effect, where the effect of one input variable (i.e., source mass) on a response variable (i.e., thickness) depends on another variable (i.e., heating current).

The regression analysis for grain size (Figure 3d) reveals the feature of interaction effect more clearly. We can no longer observe simple linear relationships between the source mass and the grain size in the 2D contour plot at an excess MAI ratio of 1 (Figure 3e,f). Depending on the heating current, the grain size either increases (heating current of 60 A) or decreases (140 A) with source mass. This is a good example of an interaction effect, where a response variable (i.e., grain size) is affected strongly by interaction terms of multiple variables (i.e., heating current × source mass). In other words, the grain size cannot be represented by a simple linear model. This is the origin of an apparently weak correlation between the grain size and the source mass from the correlation matrix plot in Figure 2, since the interaction with other variables (i.e., heating current) was neglected. Similarly, each interaction between input variables for each response variable can be effectively expressed by the interaction plot (Figure S10, Supporting Information). Overall, we have demonstrated that the multivariate regression analysis allows us to predict various film properties by modeling their complex relationships with multiple input variables which collectively define the film deposition conditions.

The goal of our study is to employ DoE for optimizing film deposition conditions for obtaining high-performance flash-evaporated perovskite photodetector devices. The DoE process allowed us to predict the responsivity values of photodetector devices via regression analysis as can be shown from a high R^2 value (Table S4, Supporting Information). In order to optimize the responsivity, the deposition condition can be simply found
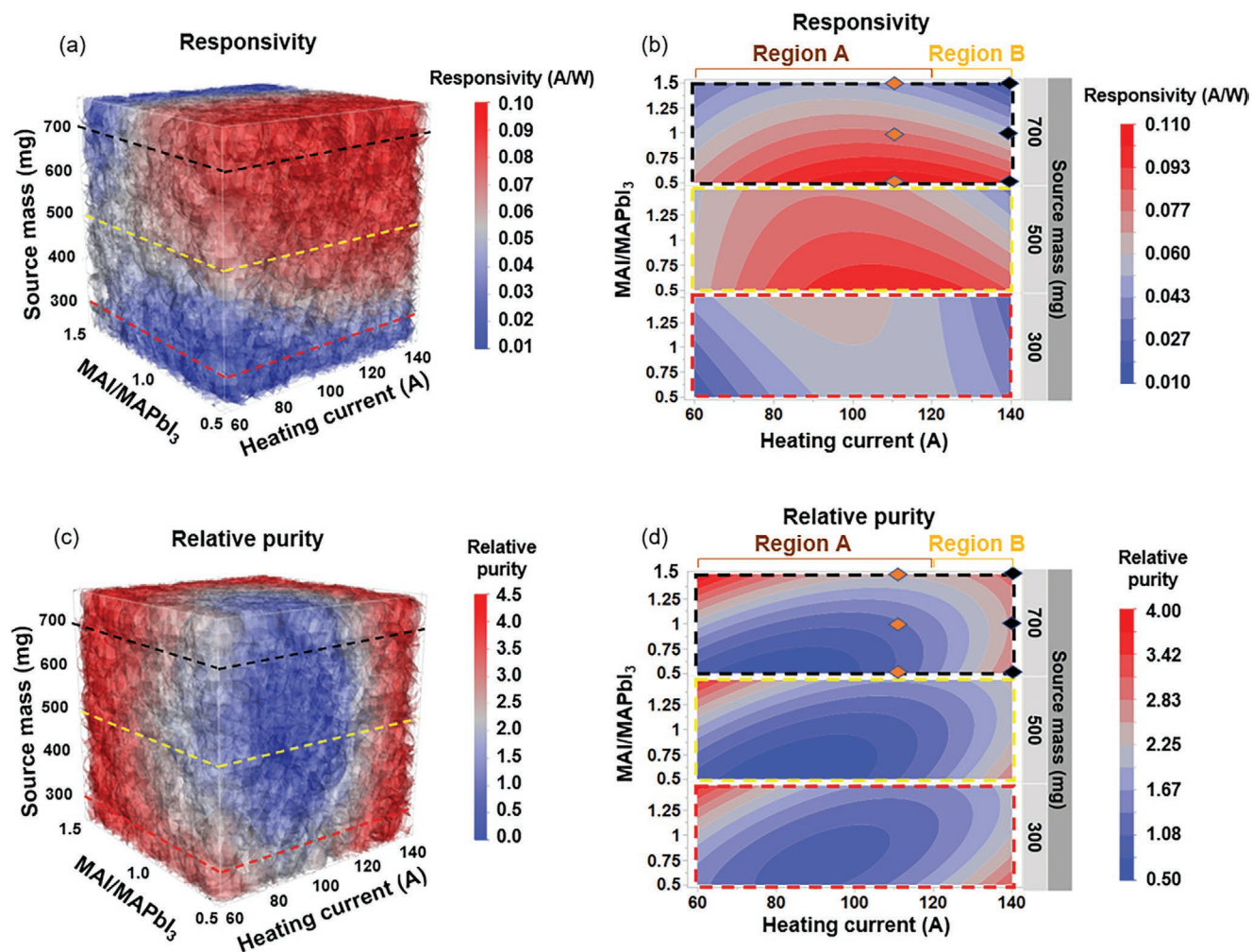
ADVANCED
SCIENCE NEWS
www.advancedsciencenews.com

ADVANCED
MATERIALS
TECHNOLOGIES
www.advmattechnol.de

Figure 4. 3D scattering plots of a) the responsivity and c) the relative purity according to the heating current, source mass, and MAI/MAPbI$_3$ from the regression analysis. Contour plots of b) responsivity and d) the relative purity are extracted from 3D scattering data (Figure 4a,c) at the source mass of 300, 500, 700 mg.

where the predicted responsivity value reaches maximum in the regression analysis result. In this way, it is possible to fabricate photodetectors with film deposition conditions predicted to achieve the maximum responsivity value without individually controlling the factors that affect responsivity, such as grain size, relative purity, and trap density. Nevertheless, it is informative to carry out a detailed correlation analysis in order to find out the main factors accountable for the optimized device performance. Therefore, we focused on extracting relationships between responsivity and other response variables for which reliable regression models with high R^2 values were obtained: thickness, relative purity, and grain size.

As shown in the 3D scattering plot (**Figure 4**a), the responsivity is predicted to increase as the source mass increases. This is expected due to the strong influence of the source mass on the deposited thickness of the perovskite film (Figure 3c). Since the tested thickness range is significantly smaller than the expected light penetration depth in MAPbI$_3$,[34] the generated photocurrent at the same input light power will attune to a similar scale with the thickness of the film. We have experimentally

confirmed the thickness scaling in the responsivity by comparing photodetector devices made with multistacked perovskite films (see Section S11, Supporting Information).

We tried to discover hidden details within the expected thickness scaling of the responsivity by looking at 2D contour plots (Figure 4b) generated from planar cross-sections of the 3D plot for the source mass of 300 mg (red dashed line cut in Figure 4a), 500 (yellow), and 700 mg (black). Figure 4c,d is the 3D scattering plots and corresponding 2D contour plots generated from the regression analysis for the relative purity of the evaporated film. When comparing Figure 4b,d as a whole, the responsivity and relative purity do not seem to have a clear correlation, which implies complexities in relating the responsivity and relative purity from the input variables. However, when it comes to a smaller deposition condition range, a noticeable correlation can be found. More specifically, if we divide the regions according to the heating current value as "Region A" from 60 to 120 A and "Region B" from 120 to 140 A (see Figure 4b,d), a negative correlation between responsivity and relative purity can be seen in Region A in the contour plot for the source mass

**ADVANCED
SCIENCE NEWS**
www.advancedsciencenews.com

**ADVANCED
MATERIALS
TECHNOLOGIES**
www.advmattechnol.de

of 700 mg (top panels of Figure 4b,d) (see Section S12 in the Supporting Information for the details of the negative correlation). This result is consistent with previous reports that the responsivity increases with incorporation of PbI_2 impurities in the perovskite film.[30,35] The origin of the different trends between the responsivity and relative purity in Region B is not entirely clear, but a finite formation of extra perovskite phases such as low dimensional perovskites[27a] by evaporating films at the high heating current values near 140 A may contribute to the discrepancy (see Section S13, Supporting Information). The grain size and responsivity showed a relatively small correlation (Section S14, Supporting Information), which may be due to a limited range of the grain size tested in our study compared to previous works.[36]

In order to experimentally confirm our regression models with actual data, we fabricated photodetectors with perovskite films evaporated under six deposition conditions at the edge of Region A and Region B (the orange and black points in Figure 4b,d). First, for the three conditions denoted as the orange points in Region A, we could confirm the negative correlation between the relative purity (Figure S16 in the Supporting Information) and the responsivity (Figure S17 in the Supporting Information), as predicted by the regression analysis, i.e., the relative purity increased and responsivity decreased as increasing the excess MAI ratio.

In addition, we further investigated the origin of the negative correlation between the relative purity of the evaporated film and the responsivity from the films deposited at these three conditions: a low relative purity film seems to contain some PbI_2 on the surface of the perovskite film suppressing nonradiative recombination near the contacts[30,35] (see more detailed experimental results and analysis in Section S15 of the Supporting Information). Second, for the other three deposition conditions denoted as black points in Region B, the relative purity of the film remained relatively constant (Figure 4d; and Figure S13 in the Supporting Information) but the responsivity decreased with the excess MAI ratio (Figure 4b; and Figure S14 in the Supporting Information), which also confirms the predictions from the regression model. The sound agreements between the experimental results for the responsivity and relative purity with the prediction of the regression models guarantee the reliability of the formulated regression models (Table S5, Supporting Information).

As the final step of the DoE process, we fabricated a photodetector device with the optimized film deposition condition and evaluated its device performance. The optimized deposition condition for maximizing the responsivity was predicted to the source mass of 650 mg, the excess MAI mol ratio of 0.5, and the heating current of 110 A (a discussion of the mathematical method to find the optimized deposition conditions can be found in Section 17, Supporting Information). For comparison, other photodetectors were also fabricated with perovskite films deposited under the conditions expected to perform worse: including the predicted worst deposition condition (the source mass of 750 mg, the excess MAI mol ratio of 1.5, and the heating current of 140 A). **Figure 5**a shows the photoelectric characteristics of photodetectors made of the perovskite films deposited under several different deposition conditions including the optimized and the worst condition. As expected,

the photocurrent was largest in the optimized photodetector and smallest in the worst condition photodetector. The responsivity of the optimized device was found to be 112.2 mA W^{-1} (σ: 20.6 mA W^{-1}), as confirmed from multiple evaluations (see Section S18, Supporting Information). This is a 98% improvement over the responsivity of the central condition photodetector, and 600% improvement over that of the worst condition photodetector. Moreover, to confirm the aforementioned influence of PbI_2 on the photodetector performance, ≈0.3% of PbI_2 was detected in the deposited film via Rietveld refinement of the X-ray diffraction pattern (see Section S19, Supporting Information).

Although the specific detectivity values of photodetector devices were not discussed previously due to low reliability of the regression model, the specific detectivity could be also significantly improved with the value for the optimized device showing an order of magnitude higher compared to that of the device fabricated under the worst deposition condition (see Section S20, Supporting Information). It is remarkable that the device performance parameters could be improved significantly by only proceeding parametric optimization of deposition conditions and without the introduction of a new deposition method or architectural improvement of the device. Finally, the device performance of each photodetector was further verified by testing with 520 nm laser illumination at various intensities under the optimized film conditions. The highest value of responsivity extracted was 0.24 A W^{-1}, which is comparable to the earlier reported values for $MAPbI_3$-based photodetectors[37] and commercial Si photodetectors (<0.2 A W^{-1}),[38] and specific detectivity of 6.62×10^{11} Jones (Figure 5c,d). Although the optimum deposition conditions acquired with our analysis may not be directly transferred to other deposition systems due to variations in experimental conditions, the methodologies demonstrated here, along with our analysis results, can be applied to any deposition systems. Furthermore, our work demonstrates the advantage of DoE process for its accuracy in the predictability of the photodetector responsivity values under various deposition conditions and the efficiency of the device optimization process which requires only a small number of experiments.

3. Conclusion

We have employed DoE approach for systematically investigating the deposition conditions and film properties of single-source flash-evaporated $MAPbI_3$ films with the aim of optimizing photodetector device performance. In total, OHP films were deposited under 15 different experimental conditions specified by three input variables—source mass, excess MAI, and heating current—selected by the Box–Behnken design to map various response variables that represent the structural and photophysical properties of the deposited films and photodetector device parameters. The correlations between the different film and device properties were investigated by using both a correlation matrix plot and regression analysis that enabled a detailed multivariate analysis. Our analysis reveals a significant interaction between the variables, which indicates a complex nature of the relationships between each film
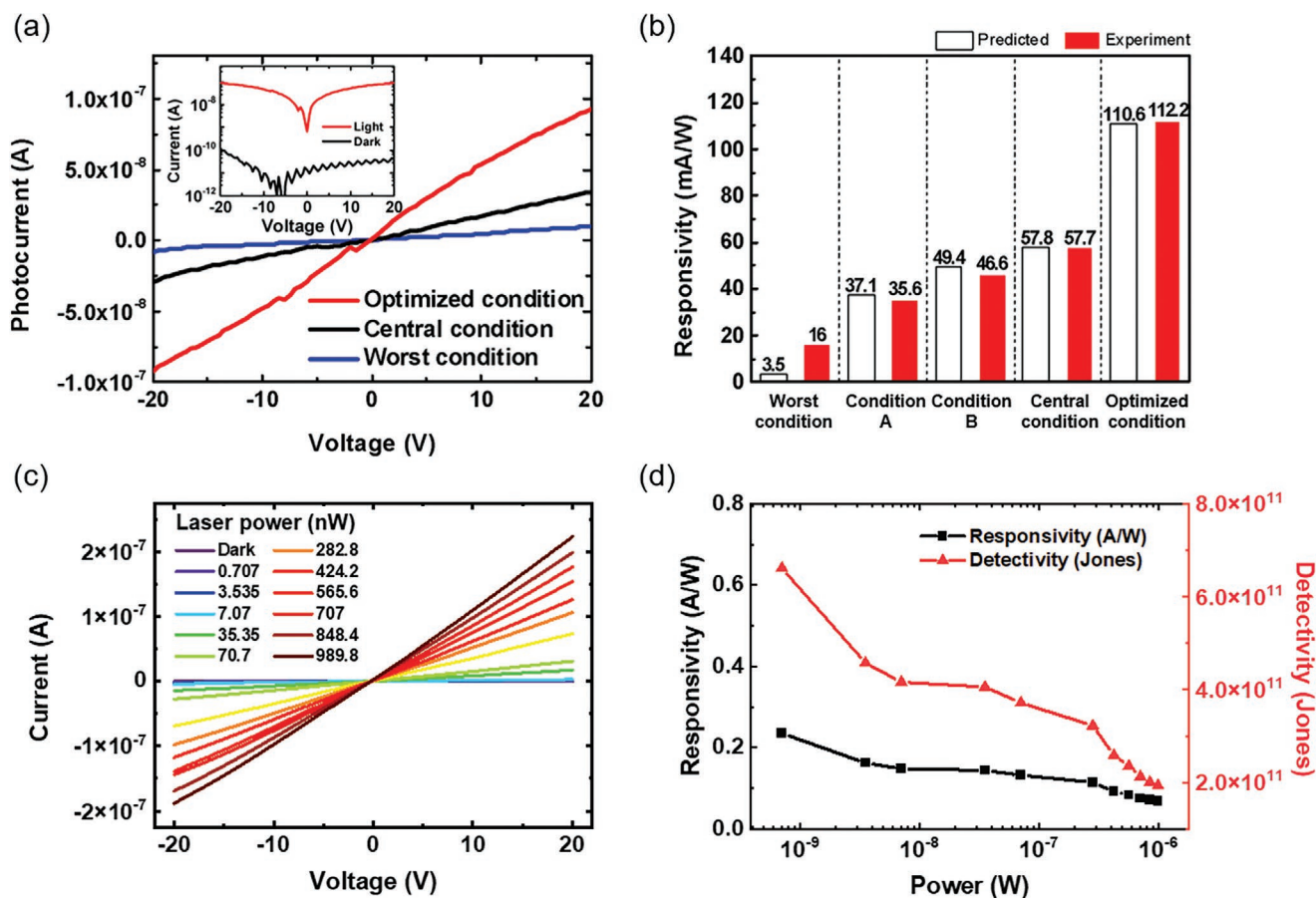
**ADVANCED
SCIENCE NEWS**

www.advancedsciencenews.com

**ADVANCED
MATERIALS
TECHNOLOGIES**

www.advmattechnol.de

Figure 5. a) *I–V* characteristics of white light illuminated photodetectors with three different MAPbI$_3$ films which are flash-evaporated under the optimized (red), central (black), and worst (blue) deposition condition. The inset shows log-scale *I–V* curves of the optimized photodetector under white light illumination (red) and dark (black) conditions. b) The predicted responsivity values from the regression model (white) and experimental values (red) under various deposition conditions. Device characteristics of the photodetectors prepared by the optimized deposition conditions. c) *I–V* characteristics under 520 nm laser illumination with different intensities. d) Photoresponsivity and detectivity of the flash evaporated MAPbI$_3$ photodetectors operated at a bias voltage of 20 V as a function of the incident laser power, both of which decrease with power, as expected.[40]

property and the input variables. Therefore, a simultaneous consideration of the variables via a multivariate approach is essential for optimizing the film deposition conditions, which cannot be achieved with a commonly practiced one-variable-at-a-time method. We have fabricated photodetector devices with the optimized deposition conditions predicted from the regression model (showing a responsivity value of 112.2 mA W^{-1}), which can be accurately predicted from the regression analysis. Overall, our work promotes DoE approach as an efficient statistical tool for optimizing perovskite film deposition conditions and a reliable route for extracting information on multidimensional relationships between material and device properties, which can be expanded to other complex optimization problems remaining in the general materials and device communities.

4. Experimental Section

Synthesis of a MAPbI$_3$ Single Crystal Powder: The MAPbI$_3$ single crystal powders were synthesized as previously reported.[22] 2.66 g of PbO (99.9% trace metal basis, Sigma-Aldrich) and 1.90 g of CH$_3$NH$_3$I

(MAI, 99.5%, Greatcellsolar) were mixed and dissolved into a mixture of 18 mL hydriodic acid (HI, 57 wt% in water, TCI-Sejin CI) solution and 2 mL hypophosphorous acid (H$_3$PO$_2$, 50 wt% in water, Thermo Fisher) solution. The solution was heated at 130 °C on a hotplate until the precipitates completely disappeared. Then, the solution was cooled at room temperature to precipitate a MAPbI$_3$ single crystal powder. The single crystal powder was filtrated with filter paper and dried in a vacuum condition.

Perovskite Film Evaporation: The thermally grown 270 nm thick SiO$_2$ on Si and glass were used as substrates. The substrates were sequentially sonicated in acetone, 2-propanol, and deionized water for 10 min each. Then, the SiO$_2$ and glass substrates were cleaned using O$_2$ plasma treatment for 120 s. For flash evaporation, the synthesized MAPbI$_3$ powder was loaded onto a tungsten boat in a vacuum chamber. The cleaned substrates were placed into the chamber at a height of 30 cm from the source material. Then, the chamber was evacuated to a pressure of Torr. The tungsten boat was rapidly heated by applying a current of 100 A. The source powder was fully evaporated within 30 s.

Characterization and Measurement: SEM: The images of the perovskite film were captured using JSM-7800F Prime at 5–10 kV.

XRD: Crystallographic structures of perovskite films were analyzed by high-resolution X-ray diffractometer technique (Rigaku Smartlab).

Rietveld Refinement: XRD patterns were subject to Rietveld refinement using the GSAS-II[39] software for phase quantification. Strong preferred

orientations of the deposited films required use of the March–Dollase function; peak broadening was treated with the domain size model due to the relatively small grain sizes (≈50 nm via SEM).

Photoluminescence (PL) spectroscopy: Steady-state PL spectra were measured using a spectrofluorometer (JASCO FP-8500) with a 520 nm excitation source.

UV–Visible Absorbance Spectroscopy: Absorbance spectra were measured using a UV/Vis spectrophotometer (PerkinElmer LAMBDA 45).

AFM: The perovskite layer surface was characterized by an atomic force microscope system (NX 10 AFM, Park Systems).

Device Fabrication: In order to fabricate photodetector, Au electrodes with a thickness of 50 nm were deposited on the prepared perovskite film by electron-beam evaporator through a shadow mask. The channel length and width of the fabricated photodetector were 50 μm and 1 mm.

Device Measurement: The perovskite photodetector characteristics were measured using a semiconductor parameter analyzer (Keithley 4200 SCS). All the measurements were performed in a vacuum environment.

Data Analysis: All data were analyzed by a statistical analysis program (SAS JMP Pro 15).

Supporting Information

Supporting Information is available from the Wiley Online Library or from the author.

Acknowledgements

Conflict of Interest

The authors declare no conflict of interest.

Data Availability Statement

Research data are not shared.

Keywords

[1] a) H. Choi, C.-K. Mai, H.-B. Kim, J. Jeong, S. Song, G. C. Bazan, J. Y. Kim, A. J. Heeger, *Nat. Commun.* **2015**, *6*, 7348; b) W. Nie, H. Tsai, R. Asadpour, J.-C. Blancon, A. J. Neukirch, G. Gupta, J. J. Crochet, M. Chhowalla, S. Tretiak, M. A. Alam, H.-L. Wang, A. D. Mohite, *Science* **2015**, *347*, 522; c) H. Tsai, W. Nie, J.-C. Blancon, C. C. Stoumpos, R. Asadpour, B. Harutyunyan, A. J. Neukirch, R. Verduzco, J. J. Crochet, S. Tretiak, L. Pedesseau, J. Even, M. A. Alam, G. Gupta, J. Lou, P. M. Ajayan, M. J. Bedzyk, M. G. Kanatzidis, A. D. Mohite, *Nature* **2016**, *536*, 312; d) W. S. Yang, J. H. Noh, N. J. Jeon, Y. C. Kim, S. Ryu, J. Seo, S. I. Seok, *Science* **2015**, *348*, 1234.

[2] a) Z.-K. Tan, R. S. Moghaddam, M. L. Lai, P. Docampo, R. Higler, F. Deschler, M. Price, A. Sadhanala, L. M. Pazos, D. Credgington, F. Hanusch, T. Bein, H. J. Snaith, R. H. Friend, *Nat. Nanotechnol.* **2014**, *9*, 687; b) H.-D. Lee, H. Kim, H. Cho, W. Cha, Y. Hong, Y.-H. Kim, A. Sadhanala, V. Venugopalan, J. S. Kim, J. W. Choi, C.-L. Lee, D. Kim, H. Yang, R. H. Friend, T.-W. Lee, *Adv. Funct. Mater.* **2019**, *29*, 1901225; c) X. Zhao, Z.-K. Tan, *Nat. Photonics* **2020**, *14*, 215; d) H. Cho, S.-H. Jeong, M.-H. Park, Y.-H. Kim, C. Wolf, C.-L. Lee, J. H. Heo, A. Sadhanala, N. Myoung, S. Yoo, S. H. Im, R. H. Friend, T.-W. Lee, *Science* **2015**, *350*, 1222; e) Y. Cao, N. Wang, H. Tian, J. Guo, Y. Wei, H. Chen, Y. Miao, W. Zou, K. Pan, Y. He, H. Cao, Y. Ke, M. Xu, Y. Wang, M. Yang, K. Du, Z. Fu, D. Kong, D. Dai, Y. Jin, G. Li, H. Li, Q. Peng, J. Wang, W. Huang, *Nature* **2018**, *562*, 249.

[3] a) B. Hwang, J.-S. Lee, *Adv. Opt. Mater.* **2019**, *7*, 1801356; b) J. C. Blancon, H. Tsai, W. Nie, C. C. Stoumpos, L. Pedesseau, C. Katan, M. Kepenekian, C. M. M. Soe, K. Appavoo, M. Y. Sfeir, S. Tretiak, P. M. Ajayan, M. G. Kanatzidis, J. Even, J. J. Crochet, A. D. Mohite, *Science* **2017**, *355*, 1288; c) Y. Fang, Q. Dong, Y. Shao, Y. Yuan, J. Huang, *Nat. Photonics* **2015**, *9*, 679; d) L. Dou, Y. Yang, J. You, Z. Hong, W.-H. Chang, G. Li, Y. Yang, *Nat. Commun.* **2014**, *5*, 5404.

[4] a) K. Kang, H. Ahn, Y. Song, W. Lee, J. Kim, Y. Kim, D. Yoo, T. Lee, *Adv. Mater.* **2019**, *31*, 1804841; b) B. Hwang, J.-S. Lee, *Sci. Rep.* **2017**, *7*, 673.

[5] a) W. Yu, F. Li, L. Yu, M. R. Niazi, Y. Zou, D. Corzo, A. Basu, C. Ma, S. Dey, M. L. Tietze, U. Buttner, X. Wang, Z. Wang, M. N. Hedhili, C. Guo, T. Wu, A. Amassian, *Nat. Commun.* **2018**, *9*, 5354; b) S. P. Senanayak, B. Yang, T. H. Thomas, N. Giesbrecht, W. Huang, E. Gann, B. Nair, K. Goedel, S. Guha, X. Moya, C. R. McNeill, P. Docampo, A. Sadhanala, R. H. Friend, H. Sirringhaus, *Sci. Adv.* **2017**, *3*, e1601935.

[6] a) L. Niu, X. Liu, C. Cong, C. Wu, D. Wu, T. R. Chang, H. Wang, Q. Zeng, J. Zhou, X. Wang, W. Fu, P. Yu, Q. Fu, S. Najmaei, Z. Zhang, B. I. Yakobson, B. K. Tay, W. Zhou, H. T. Jeng, H. Lin, T. C. Sum, C. Jin, H. He, T. Yu, Z. Liu, *Adv. Mater.* **2015**, *27*, 7800; b) C. Lan, R. Dong, Z. Zhou, L. Shu, D. Li, S. Yip, J. C. Ho, *Adv. Mater.* **2017**, *29*, 1702759.

[7] a) C. Momblona, L. Gil-Escrig, E. Bandiello, E. M. Hutter, M. Sessolo, K. Lederer, J. Blochwitz-Nimoth, H. J. Bolink, *Energy Environ. Sci.* **2016**, *9*, 3456; b) D. B. Mitzi, M. T. Prikas, K. Chondroudis, *Chem. Mater.* **1999**, *11*, 542.

[8] Y. Chen, L. Zhang, Y. Zhang, H. Gao, H. Yan, *RSC Adv.* **2018**, *8*, 10489.

[9] J. Ávila, C. Momblona, P. P. Boix, M. Sessolo, H. J. Bolink, *Joule* **2017**, *1*, 431.

[10] M. Era, T. Hattori, T. Taira, T. Tsutsui, *Chem. Mater.* **1997**, *9*, 8.

[11] J. Yin, H. Qu, J. Cao, H. Tai, J. Li, N. Zheng, *J. Mater. Chem. A* **2016**, *4*, 13203.

[12] G. Li, J. Y. L. Ho, M. Wong, H.-S. Kwok, *Phys. Status Solidi RRL* **2016**, *10*, 153.

[13] H. Xu, Y. Wu, F. Xu, J. Zhu, C. Ni, W. Wang, F. Hong, R. Xu, F. Xu, J. Huang, L. Wang, *RSC Adv.* **2016**, *6*, 48851.

[14] a) M. Sessolo, C. Momblona, L. Gil-Escrig, H. J. Bolink, *MRS Bull.* **2015**, *40*, 660; b) M. J. Crane, D. M. Kroupa, J. Y. Roh, R. T. Anderson, M. D. Smith, D. R. Gamelin, *ACS Appl. Energy Mater.* **2019**, *2*, 4560.

[15] a) P. Du, J. Li, L. Wang, J. Liu, S. Li, N. Liu, Y. Li, M. Zhang, L. Gao, Y. Ma, J. Tang, *ACS Appl. Mater. Interfaces* **2019**, *11*, 47083; b) M. Liu, M. B. Johnston, H. J. Snaith, *Nature* **2013**, *501*, 395.

[16] L. K. Ono, S. Wang, Y. Kato, S. R. Raga, Y. Qi, *Energy Environ. Sci.* **2014**, *7*, 3989.

[17] a) D. Yang, Z. Yang, W. Qin, Y. Zhang, S. Liu, C. Li, *J. Mater. Chem. A* **2015**, *3*, 9401; b) C.-W. Chen, H.-W. Kang, S.-Y. Hsiao, P.-F. Yang,

K.-M. Chiang, H.-W. Lin, *Adv. Mater.* **2014**, *26*, 6647; c) B. Hwang, J.-S. Lee, *Adv. Mater.* **2017**, *29*, 1701048.

[18] a) P. Fan, D. Gu, G.-X. Liang, J.-T. Luo, J.-L. Chen, Z.-H. Zheng, D.-P. Zhang, *Sci. Rep.* **2016**, *6*, 29910; b) G. Longo, L. Gil-Escrig, M. J. Degen, M. Sessolo, H. J. Bolink, *Chem. Commun.* **2015**, *51*, 7376.

[19] K. B. Lohmann, J. B. Patel, M. U. Rothmann, C. Q. Xia, R. D. J. Oliver, L. M. Herz, H. J. Snaith, M. B. Johnston, *ACS Energy Lett.* **2020**, *5*, 710.

[20] J. Antony, *Design of Experiments for Engineers and Scientists*, Elsevier **2014**.

[21] P. Tyagi, T. W. David, V. D. Stoichkov, J. Kettle, *Sol. Energy* **2019**, *193*, 12.

[22] W. Lee, J. Lee, H.-D. Lee, J. Kim, H. Ahn, Y. Kim, D. Yoo, J. Lee, T.-W. Lee, K. Kang, T. Lee, *Sci. Rep.* **2020**, *10*, 18781.

[23] a) R. F. Gunst, *Technometrics* **1996**, *38*, 284; b) G. E. P. Box, N. R. Draper, in *Response Surfaces, Mixtures, and Ridge Analyses*, John Wiley & Sons **2007**.

[24] S. L. C. Ferreira, R. E. Bruns, H. S. Ferreira, G. D. Matos, J. M. David, G. C. Brandão, E. G. P. da Silva, L. A. Portugal, P. S. dos Reis, A. S. Souza, W. N. L. dos Santos, *Anal. Chim. Acta* **2007**, *597*, 179.

[25] J. L. Richards, P. B. Hart, L. M. Gallone, *J. Appl. Phys.* **1963**, *34*, 3418.

[26] a) Y. Ando, Y. Ohishi, K. Suzuki, A. Suzuki, T. Oku, *AIP Conf. Proc.* **2018**, *1929*, 020003; b) L. McCusker, R. Von Dreele, D. Cox, D. Louër, P. Scardi, *J. Appl. Crystallogr.* **1999**, *32*, 36; c) R. Von Dreele, *J. Appl. Crystallogr.* **1997**, *30*, 517.

[27] a) Z. Song, S. C. Watthage, A. B. Phillips, B. L. Tompkins, R. J. Ellingson, M. J. Heben, *Chem. Mater.* **2015**, *27*, 4612; b) M. K. Daniel, J. C. Matthew, R. G. Daniel, *Proc. SPIE* **2019**, *11084*, 110840J.

[28] a) Y. Fang, A. Armin, P. Meredith, J. Huang, *Nat. Photonics* **2019**, *13*, 1; b) F. P. García de Arquer, A. Armin, P. Meredith, E. H. Sargent, *Nat. Rev. Mater.* **2017**, *2*, 16100.

[29] Y. Kanemitsu, *J. Mater. Chem. C* **2017**, *5*, 3427.

[30] D. H. Cao, C. C. Stoumpos, C. D. Malliakas, M. J. Katz, O. K. Farha, J. T. Hupp, M. G. Kanatzidis, *APL Mater.* **2014**, *2*, 091101.

[31] S. Hinds, L. Levina, E. J. D. Klem, G. Konstantatos, V. Sukhovatkin, E. H. Sargent, *Adv. Mater.* **2008**, *20*, 4398.

[32] R. Taylor, *J. Diagn. Med. Sonography* **1990**, *6*, 35.

[33] L. Leng, T. Zhang, L. Kleinman, W. Zhu, *J. Phys. Conf. Ser.* **2007**, *78*, 012084.

[34] Z. Shi, Y. Zhang, C. Cui, B. Li, W. Zhou, Z. Ning, Q. Mi, *Adv. Mater.* **2017**, *29*, 1701656.

[35] a) T. J. Jacobsson, J.-P. Correa-Baena, E. Halvani Anaraki, B. Philippe, S. D. Stranks, M. E. F. Bouduban, W. Tress, K. Schenk, J. Teuscher, J.-E. Moser, H. Rensmo, A. Hagfeldt, *J. Am. Chem. Soc.* **2016**, *138*, 10331; b) Y. C. Kim, N. J. Jeon, J. H. Noh, W. S. Yang, J. Seo, J. S. Yun, A. Ho-Baillie, S. Huang, M. A. Green, J. Seidel, T. K. Ahn, S. I. Seok, *Adv. Energy Mater.* **2016**, *6*, 1502104; c) L. Wang, C. McCleese, A. Kovalsky, Y. Zhao, C. Burda, *J. Am. Chem. Soc.* **2014**, *136*, 12205.

[36] T. Geske, J. Li, M. Worden, X. Shan, M. Chen, S. G. R. Bade, Z. Yu, *Adv. Funct. Mater.* **2017**, *27*, 1702180.

[37] a) C. Bao, W. Zhu, J. Yang, F. Li, S. Gu, Y. Wang, T. Yu, J. Zhu, Y. Zhou, Z. Zou, *ACS Appl. Mater. Interfaces* **2016**, *8*, 23868; b) F. Bai, J. Qi, F. Li, Y. Fang, W. Han, H. Wu, Y. Zhang, *Adv. Mater. Interfaces* **2018**, *5*, 1701275; c) R. Gegevičius, M. Treideris, V. Pakštas, M. Franckevičius, V. Gulbinas, *Adv. Electron. Mater.* **2018**, *4*, 1800114; d) H. Wei, H. Ma, M. Tai, Y. Wei, D. Li, X. Zhao, H. Lin, S. Fan, K. Jiang, *RSC Adv.* **2017**, *7*, 34795.

[38] a) F. Guo, B. Yang, Y. Yuan, Z. Xiao, Q. Dong, Y. Bi, J. Huang, *Nat. Nanotechnol.* **2012**, *7*, 798; b) K. Wang, C. Wu, D. Yang, Y. Jiang, S. Priya, *ACS Nano* **2018**, *12*, 4919.

[39] B. H. Toby, R. B. Von Dreele, *J. Appl. Crystallogr.* **2013**, *46*, 544.

[40] C. Ji, P. Wang, Z. Wu, Z. Sun, L. Li, J. Zhang, W. Hu, M. Hong, J. Luo, *Adv. Funct. Mater.* **2018**, *28*, 1705467.